THE JOURNAL OF PHYSICAL CHEMISTRY C

pubs.acs.org/JPCC Article

Isomeric Thiolate Monolayer Protected Au_{92} and Au_{102} Nanomolecules

Naga Arjun Sakthivel, Luca Sementa, Bokwon Yoon, Uzi Landman,* Alessandro Fortunelli,* and Amala Dass*

Cite This: *J. Phys. Chem. C* 2020, 124, 1655−1666 Read Online

ACCESS | Metrics & More | Article Recommendations | Supporting Information

ABSTRACT: We report the results of a study of the isomeric thiolate monolayer capping of two gold nanocluster molecules, namely Au_{92} and Au_{102}, both protected by 44 4-*tert*-butylbenzene thiolate (TBBT) ligands. The finding of an isomeric monolayer of the same ligand in a series of metal nanocluster molecules in this large size range is unprecedented. Au_{92} and Au_{102} possess entirely different structures and properties. The Au_{92} has an 84 atom face centered cubic (FCC) core whereas Au_{102} has a 79 atom Marks-decahedral core. Nevertheless, despite the metal core structural diversity and the complexities of the interfacial staples, both of these gold nanocluster molecules have the same number of ligands. The Au_{92} core is protected by 28 bridging ligands and 8 monomeric staple motifs whereas Au_{102} is protected by 19 monomeric and 2 dimeric staple motifs. The Au_{92} and Au_{102} cores have cuboidal and globular structures, respectively. As a result, Au_{92} has longer {100} facets and exhibits $c(2 \times 2)$ monolayer arrangement for bridging ligands similar to what has been observed on {100} facets of bulk gold, whereas Au_{102} has only staple motifs. We prepared the Au_{102} in TBBT series using a ligand-exchange-based approach and characterized them by mass spectrometry and UV−vis spectroscopy. Mass spectrometry revealed that the compound has a mixture of isoelectronic species with the formula of $Au_{102}(TBBT)_{44}$, $Au_{103}(TBBT)_{45}$, and $Au_{104}(TBBT)_{46}$. Concurrent first-principles electronic structure computational studies provide insights into the stability and nature of these two isomeric-monolayer capped gold nanomolecules.

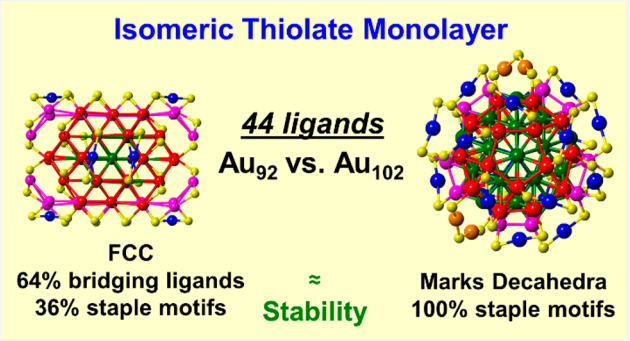

INTRODUCTION

The facile synthesis of stable, thiolate protected gold nanoparticles[1] and their subsequent identification to be molecules[2] with unique electrochemical[3−6] and optical properties[7−12] drew interest from researchers across diverse areas of scientific research. Investigations of Au_{102} and Au_{25} gold nanomolecules further triggered the field's growth significantly, following the reports in 2007 and 2008 about their X-ray crystallographic structures, respectively.[13,14] The Au_{102} system has been studied widely with applications in drug delivery and catalysis.[13,15−23] It has been synthesized with water-soluble and organo-soluble ligands.[24−26] In the case of organo-soluble ligands, thiophenolate ligands support the $Au_{102}(SR)_{44}$ molecular formula and has an electrochemical gap of ∼0.6 V, which is in reasonable agreement with the theoretically computed band gap.[25] $Au_{99}(SR)_{42}$, which is a stable size in the thiophenolate protected series of nanomolecules, remains to be crystallographically studied.[26,27] In contrast, in the case of phenylethanethiolate (aliphatic-like) and aliphatic thiolate ligands, a mixture of sizes were found: ($Au_{103}(SR)_{45}$, $Au_{104}(SR)_{45}$, $Au_{104}(SR)_{46}$ and $Au_{105}(SR)_{46}$).[28,29] A wide range of Marks decahedral (m-Dh)[30] and decahedral (Dh) nanomolecules have been discovered since then in gold and silver nanomolecules systems with 102−374 metal atoms.[31−37] Several other polyhedral structures such as icosahedra, anticuboctahedra, and truncated octahedra, with interesting properties and applications have been discovered.[38−50]

Distinct ligands form distinct series of gold-based nanomolecules (AuNMs) sizes, each characterized by a precise number of gold atoms and ligands.[51] To date, there is only one known occurrence of two cluster sizes (that is, with different number of gold atoms) having an isomeric ligand count, namely, the phenylethanethiolate-capped Au_{38} and Au_{40} clusters protected by 24 ligands.[52]

The 4-*tert*-butylbenzenethiolate (TBBT, SPh-*t*Bu) protected series of AuNMs comprises: $Au_{28}(SR)_{20}$, $Au_{36}(SR)_{24}$, $Au_{44}(SR)_{28}$, $Au_{52}(SR)_{32}$, $Au_{92}(SR)_{44}$, $Au_{133}(SR)_{52}$, and $Au_{279}(SR)_{84}$.[31] We have prepared a mixture of isoelectronic

Received: September 18, 2019
Revised: December 17, 2019
Published: December 24, 2019

https://dx.doi.org/10.1021/acs.jpcc.9b08846
J. Phys. Chem. C 2020, 124, 1655−1666

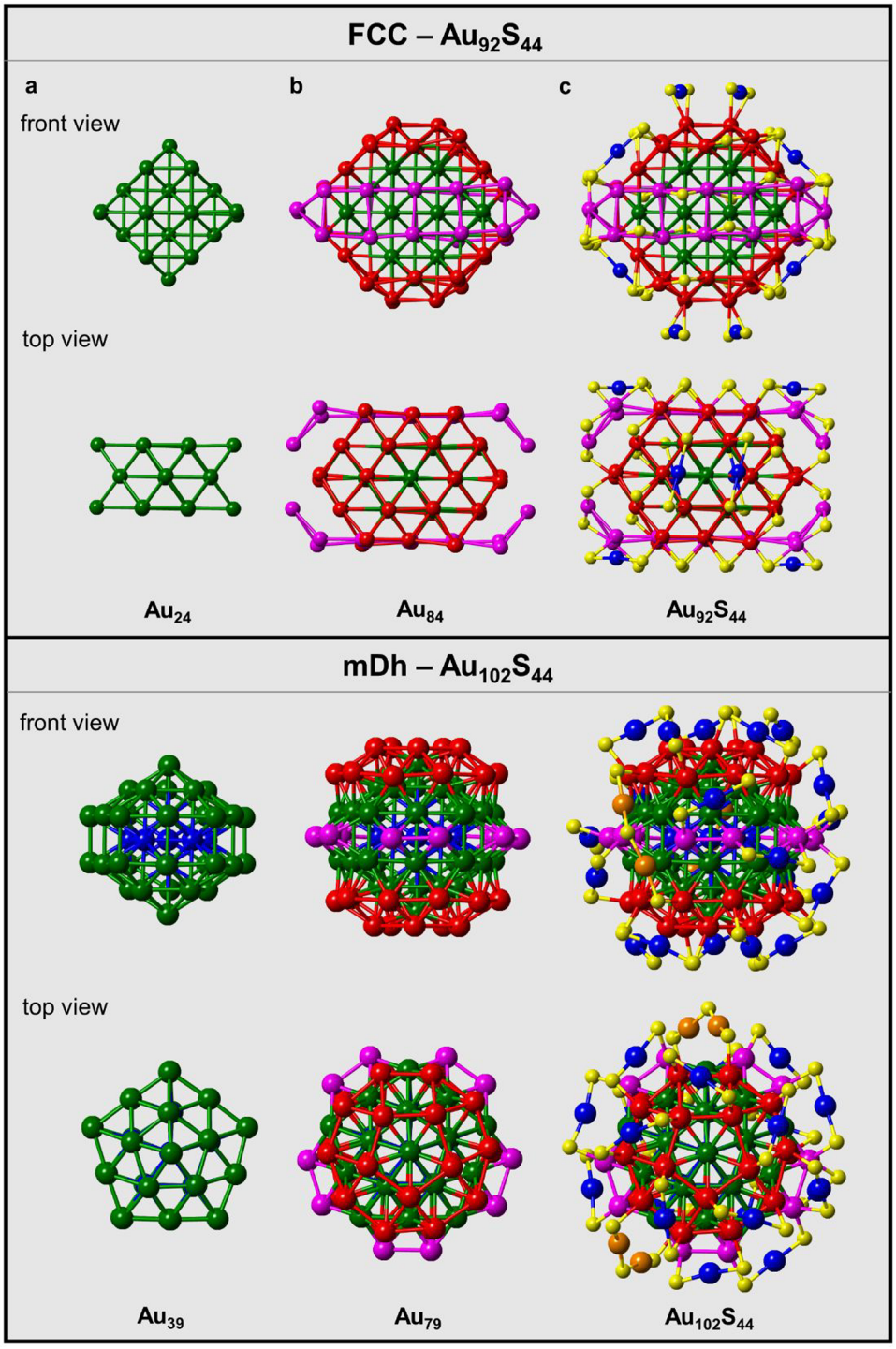

Figure 1. X-ray crystal structures of Au_{92} and Au_{102}: (a) core-centered atoms, (b) core atoms, and (c) total structure. Staples: blue, monomeric Au; orange, dimeric Au; yellow, sulfur. C and H atoms are excluded for clarity.

stable sizes with a molecular formula of $Au_{102}(TBBT)_{44}$, $Au_{103}(TBBT)_{45}$, and $Au_{104}(TBBT)_{46}$ evidenced by mass spectra. It is intriguing and unprecedented that with the same number of thiolate groups, two core-sizes (Au_{92} (refs 53 and 54) and Au_{102}) exist in the same series, with the two clusters differing by 10 Au atoms, and exhibiting two entirely different structures. A difference of 50 Au atoms and isomeric monolayer has been observed between two different series; $Au_{329}(SR)_{84}$ in the phenylethanethiolate series and $Au_{279}(SR)_{84}$ in the TBBT series.[55] The $Au_{102}(SR)_{42}$ and $Au_{104}(SR)_{46}$ compounds with closely related composition to $Au_{102}(SR)_{44}$ (ref 13) have been modeled computationally and shown to possess a m-Dh 79 atom core as well, with differences in the staple motif configurations.[16] Later, the $Au_{104}(SR)_{46}$ composition has been identified experimentally as well.[28,29] We predict that the $Au_{102}(TBBT)_{44}$, $Au_{103}(TBBT)_{45}$ and $Au_{104}(TBBT)_{46}$ would also have a m-Dh 79 atom core–shell structure similar to its analogs protected by $-SC_6H_4COOH$ and $-SC_{10}H_7$.[13,56] In the case of $Au_{102}(SR)_{44}$, the stability of the nanomolecule has been

https://dx.doi.org/10.1021/acs.jpcc.9b08846
J. Phys. Chem. C 2020, 124, 1655−1666

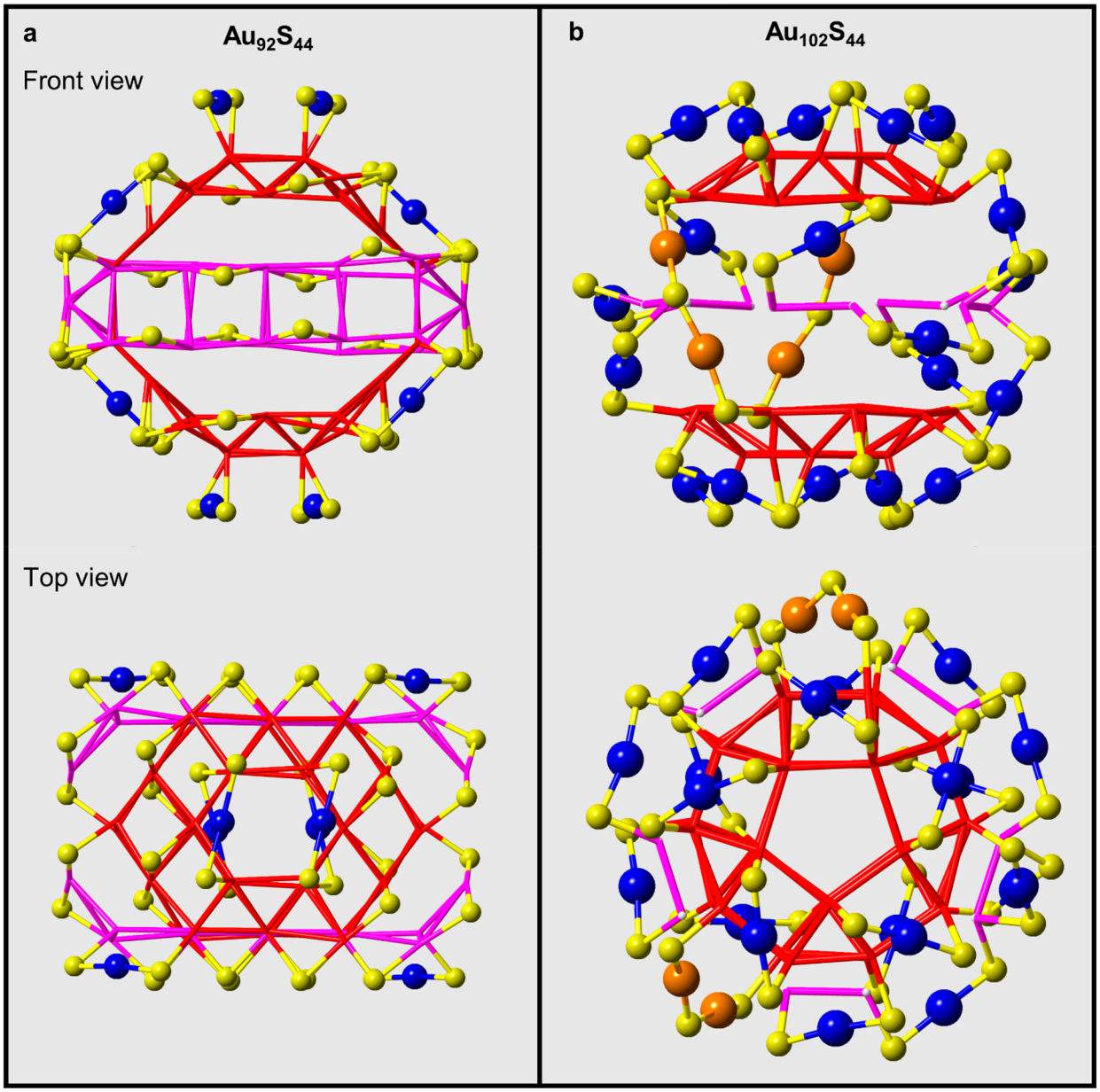

Figure 2. Isomeric TBBT monolayer on (a) Au_{92} and (b) Au_{102}. Staples: blue, monomeric Au, orange, dimeric Au, and yellow, sulfur. Surface Au atoms on {111} (red) and {100} (magenta) facets. Core-centered Au atoms, C, and H are excluded for clarity.

ascribed to the magic 58-electron closed shell, but recent experimental studies indicate that geometric stability of the mDh structural motif could also be a major factor in its stability.[56,57] It is pertinent to remark here that although electronic shell closing is certainly a factor contributing to the stability of a number of nanocluster systems, there are also a number of stable AuNMs that do not exhibit "magic" electron-shell closing, including: $Au_{30}(SR)_{18}$, $Au_{36}(SR)_{24}$, $Au_{38}(SR)_{24}$, $Au_{130}(SR)_{50}$, $Au_{133}(SR)_{52}$, and $Au_{144}(SR)_{60}$.[31]

Here, we report the results of structural and computational explorations of the Au_{92} and Au_{102} nanomolecules capped by isomeric thiolate monolayers. *Despite the structural diversities in the metal core and the complexities of the interfacial staples, both of these AuNMs have the same number of ligands.* We also report here the first preparation of TBBT-protected Au_{102}. The product has been analyzed by mass spectrometry (matrix-assisted laser desorption ionization (MALDI) and electrospray ionization (ESI) mass spectrometry) to determine the composition, while optical absorption spectroscopy has been employed to determine the difference in electronic properties between the Au_{92} and Au_{102} nanomolecules. Theoretical studies were performed to provide insights into the electronic structure and stability of the two sizes with isomeric monolayer but possessing drastically different structures.

RESULTS AND DISCUSSION

$Au_{92}(TBBT)_{44}$ nanomolecule has an 84 Au atom FCC core protected by eight monomeric staple units (−SR−Au−SR) and 28 bridging ligands (−Au−SR−Au−). The 84 atom core has an arrangement of $Au_2@Au_{18}$+$Au_4@Au_{60}$ atoms. Au_2 forms the center of the interpenetrating bicuboctahedral structure ($Au_2@Au_{18}$), followed by four Au atoms on the four trapezoidal {111} facets on the bicuboctahedra (Figure 1). The Au_{24} core is covered by the 60 Au atoms layer which is

https://dx.doi.org/10.1021/acs.jpcc.9b08846
J. Phys. Chem. C 2020, 124, 1655−1666

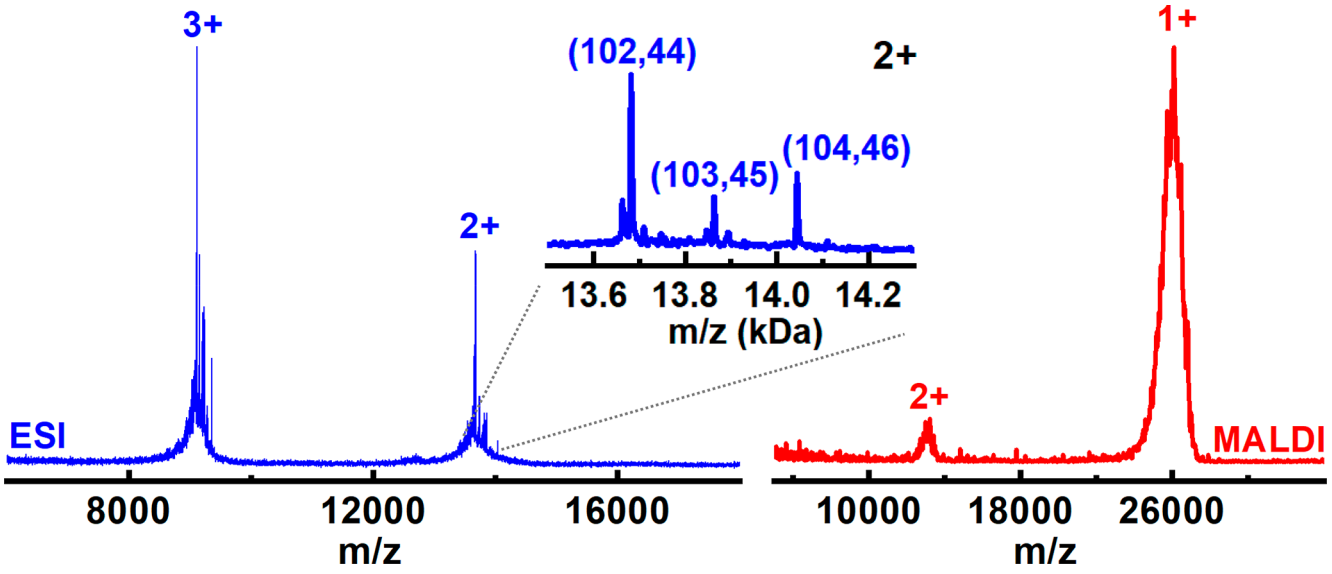

Figure 3. MALDI and ESI mass spectra of $Au_{102-104}(TBBT)_{44-46}$ nanomolecules. MALDI spectra (red) reveals the 1+ and 2+ charge states at ~26.2 kDa and ~13 kDa, respectively. ESI spectra (blue) reveals the 2+ and 3+ charge state for $Au_{102-104}(TBBT)_{44-46}$ nanomolecules. Inset shows the zoom-in in the 2+ m/z region showing the peaks for three isoelectronic species with (Au,TBBT) = (102,44), (103,45), and (104,46).

then protected the TBBT ligand monolayer. The $Au_{102}(SR)_{44}$ structure has a 79 atom mDh core protected by 19 monomeric staples and 2 dimeric staples (Figure 1). The 79 atom mDh core has an Au_7 decahedra @ Au_{32} Ino's decahedra (iDh) core with Au_{10} along the {100} facets of the iDh forms the Au49 mDh core. Then, 2x Au_{15} caps on the poles of the core forms the m-Dh 79 atom core. The 60 Au atoms layer in Au_{92} can be viewed as a 2x 18 Au atom caps on the poles and 2x 12 Au atom belt along the equatorial position of the core analogous to the 2x Au_{15} caps and Au_{10} belt along the equatorial position in Au_{102} (Figure 1).

Figure 2 illustrates the differences in arrangement of thiolate monolayer on Au_{92} and Au_{102} nanomolecules. In Au_{92}, two monomeric staples are located on both the poles of the core in a 2-fold symmetry and 2 monomeric staples from both poles' trapezoidal {111} facet connects to the equatorial belt. The bridging thiolate groups are arranged in a $c(2 \times 2)$ arrangement on the {100} facets like thiolate groups on the {100} facets of bulk gold.[31,58] In Au_{92}, ~ 64% of the ligands are in bridging configuration and the rest in monomeric staple motifs. In Au_{102}, the 15 atom caps on the poles have five monomeric staple motifs arranged in a 5-fold rotational symmetry protecting 10 Au atoms (Figure 2). Out of five tetrahedral wedges of the decahedra, three wedges has three monomeric staples from each pole anchoring the six out of ten Au atoms on the {100} facets of the Au_{39} (iDh). The remaining four atoms on the equatorial belt is protected by two monomeric staples. Two dimeric staple motifs protect the remaining two Au atoms on both the poles.

Mass Spectrometry. The composition of $Au_{102-104}(TBBT)_{44-46}$ nanomolecules were studied by matrix-assisted laser desorption ionization (MALDI) mass spectrometry and electrospray ionization (ESI) mass spectrometry. MALDI-MS data reveals the 1+ and 2+ charge state of the compound with broad peak due to fragmentation (Figure 3). It also indicates that no neighboring sizes other than $Au_{102-104}$ are present. ESI-MS was performed using THF as solvent and no Cs^+ was added. The analyte ionized in 2+ and 3+ charge state peaks and the molecular composition was determined by deconvoluting the charge state peaks to get the molecular weight. The m/z peaks for 2+ and 3+ charge states of $Au_{102}(TBBT)_{44}$, $Au_{103}(TBBT)_{45}$, and $Au_{104}(TBBT)_{46}$ were observed at the following m/z values, 13 681 Da, 13 861 Da, and 14 044 and 9121 Da, 9241 Da, and 9361 Da, respectively. Figure 3 inset shows the 2+ of $Au_{102}(TBBT)_{44}$, $Au_{103}(TBBT)_{45}$, and $Au_{104}(TBBT)_{46}$.

UV–Vis Spectroscopy. Figure 4 reports the optical absorption spectrum of $Au_{102-104}$ in comparison with the two neighboring sizes in TBBT series, Au_{92} and Au_{133}. Au_{92} has absorption features at 440, 660, and 850 nm. Au_{133} has features at 430, 510, and 710 nm. $Au_{102-104}$ species on the other hand do not exhibit distinct bands.

Energy Decomposition and System Comparison Analyses. To compare the relative stability of $Au_{92}(TBBT)_{44}$ vs $Au_{102}(TBBT)_{44}$ we resort to computational modeling, employing our previously proposed energy decomposition (fragmentation)[59] and system comparison[60] analysis protocols that we have successfully used in previous work.[61−63] To this purpose, we use first-principles simulations based on density functional theory (DFT).

Our analysis protocols need structural information on the considered systems. For the equilibrium structure of $Au_{92}(TBBT)_{44}$ we used the crystallographic data available in ref 54. Since no crystallographic data are available for $Au_{102}(TBBT)_{44}$, we created its structure by taking the coordinates of $Au_{102}(p\text{-}MBA)_{44}$ from ref.[13] and by replacing the carboxylic groups with *tert*-butyl groups via a docking procedure which ensures that there are no overlapping atoms in the resulting configuration. The initial geometries of both these systems were then subjected to density-functional-tight-binding (DFTB) molecular dynamics (MD) simulations, lasting 3 ps at 400 K during which the coordinates of the Au and S atoms were left frozen to the initial geometry. The MD runs were followed by DFT relaxations without geometrical constraints. The thus-generated coordinates are provided in the Supporting Information.

Local geometry relaxations at DFT level and DFTB-MD runs were performed by employing the CP2K code[64] whose

https://dx.doi.org/10.1021/acs.jpcc.9b08846
J. Phys. Chem. C 2020, 124, 1655−1666

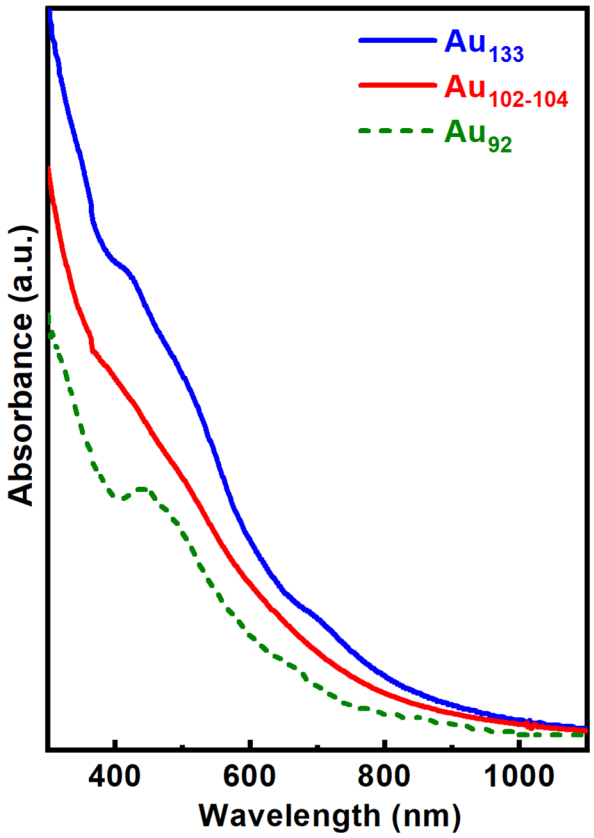

Figure 4. UV−vis absorption spectra of $Au_{102-104}(TBBT)_{44-46}$ nanomolecules (red, solid) compared with the $Au_{92}(TBBT)_{44}$ (olive, dash) and $Au_{133}(TBBT)_{44}$ (blue, solid).

DFT algorithms are based on a hybrid Gaussian/plane-wave scheme (GPW). We resorted to pseudopotentials derived by Goedecker, Teter, and Hutter[65] for describing the core electrons of all atoms, and DZVP basis sets[66] for representing the DFT Kohn−Sham valence orbitals. The cutoff for the auxiliary plane wave representation of the density was 400 Ry. Calculations were performed spin-unrestricted. The semi-empirical Grimme-D3 correction[67] was added to Perdew−Burke−Ernzerhof (PBE)[68] exchange and correlation (xc-) functional to take into account dispersion interactions. In the DFTB calculations, we used the parameters from ref 69. Time integration steps of 1 fs were used during the MD runs, and the temperature was controlled by Nosé−Hoover chain thermostats.[70]

For simplicity, we limited our analysis to electronic energies only (corresponding to 0 K ideal conditions, no entropic effects). Our analysis protocols foresee calculating the DFT energetics of the complete clusters and of a series of intermediate species to shed insight into the relative energetic stability of clusters with different stoichiometry [here, $Au_{92}(TBBT)_{44}$ vs $Au_{102}(TBBT)_{44}$] and its decomposition into separate, physically meaningful energy contributions. A full report of our results is listed in Table S1 of the Supporting Information.

We recall that our fragmentation analysis tool[59] corresponds to calculating and comparing the reaction energy of the following fragmentation, atomization, and ligand separation processes, for the two $Au_N(TBBT)_{44}$ species:

$$Au_{92}(TBBT)_{44} \rightarrow Au_{92} + (TBBT)_{44}^{crown\text{-}Au_{92}} \quad \text{fragmentation}$$

$$\Delta E^{fragm} = 4.336 \text{ au}$$

$$Au_{92} \rightarrow 92Au \quad \text{atomization} \quad \Delta E^{atmz}/N = 0.09288 \text{ au}$$

$$(TBBT)_{44}^{crown\text{-}Au92} \rightarrow 44(TBBT)_{relax} \quad \text{ligand separation}$$

$$\Delta E^{ligsep} = 1.458 \text{ au}$$

$$Au_{102}(TBBT)_{44} \rightarrow Au_{102} + (TBBT)_{44}^{crown} \quad \text{fragmention}$$

$$\Delta E^{fragm} = 4.313 \text{ au}$$

$$Au_{102} \rightarrow 102Au \quad \text{atomization} \quad \Delta E^{atmz}/M = 0.09431 \text{ au}$$

$$(TBBT)_{44}^{crown-Au_{102}} \rightarrow 44(TBBT)_{relax} \quad \text{ligand separation}$$

$$\Delta E^{ligsep} = 1.307 \text{ au}$$

whereas our system comparison analysis tool[60] investigates cluster interconversion via different steps that in the present case simplify to a metal addition reaction:

$$Au_N(TBBT)_{44} + 10\mu[Au] \rightarrow Au_{N+10}(TBBT)_{44} \quad \text{metal addition}$$

$$\Delta E^{interconv}$$

To evaluate this last reaction energy we need the chemical potential of Au, μ[Au], which can be assumed to coincide under the given experimental conditions with the atomization energy per atom of the Au-core, $\Delta E^{atmz}/N$, similar in the present case for $Au_{92}(TBBT)_{44}$ and $Au_{102}(TBBT)_{44}$: $\mu[Au] = \Delta E^{atmz}/N = 0.09288-0.09431$ au.

By using the values of total energies from Table S1 and the chemical potential of Au estimated as described above, we then calculate the cluster interconversion energy as $\Delta E^{interconv}[Au_{92}(TBBT)_{44} \rightarrow Au_{102}(TBBT)_{44}] = 0.0288-0.0431$ au, i.e., 0.78−1.17 eV. We thus arrive at our main conclusion that, despite the great structural differences between $Au_{92}(TBBT)_{44}$ and $Au_{102}(TBBT)_{44}$, these two species exhibit a similar electronic stability, with $Au_{92}(TBBT)_{44}$ more stable than $Au_{102}(TBBT)_{44}$ by roughly 1 eV. This relatively small energy difference in such large and complex compounds is striking, and confirms the great freedom in morphology and stoichiometry of nanomolecules in this nonscalable size régime. It is also in tune with the experimental observation that both clusters can exist and be successfully synthesized.

It can be noted that $Au_{92}(TBBT)_{44}$ is more stable than $Au_{102}(TBBT)_{44}$ *despite the 58-electron electronic shell closure* in the latter species. Indeed, analyzing Table S1 in more detail, one can see that the similarity in formation energy of the two MPC arises from a compensation between ligand−ligand interaction, stronger in $Au_{92}(TBBT)_{44}$ by ≈0.15 au, and Au-core atomization, which favors $Au_{102}(TBBT)_{44}$ and is connected with its electronic-shell closure effect. Ligand−ligand separation energy is practically the same for TBBT thiolate ligands and their hydrogenated TBBT-H counterparts, proving that chemical bonding between S atoms in the ligand crown does not play a role, while dispersion terms contribute by only 0.03 eV to the difference in ligand−ligand interaction, hence suggesting that phenyl−phenyl $\pi-\pi$ and T-stackings interactions[60] are mainly responsible for the enhanced stability of $Au_{92}(TBBT)_{44}$. Clearly, this kind of stabilization will depend on solvent and entropic effects[59] (provisionally neglected here).

https://dx.doi.org/10.1021/acs.jpcc.9b08846
J. Phys. Chem. C 2020, 124, 1655−1666

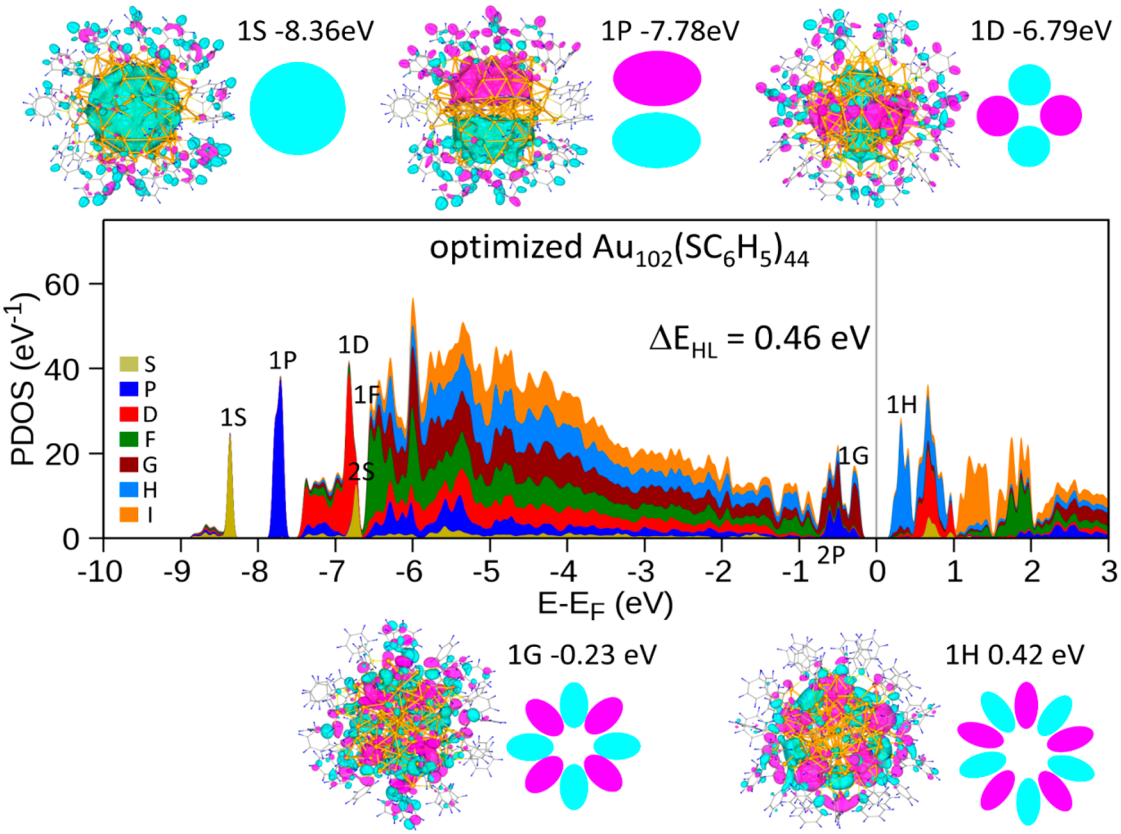

Figure 5. Calculated projected densities of states (PDOS) for $Au_{102}(S\text{-phenyl})_{44}$ and selected iso-surfaces of superatom orbitals (the two colors correspond to different signs of the wave function). We also include schematic illustrations of the orbitals' nodal structures. The various angular momenta contributions are displayed in different colors, as given in the inset.

Finally, to test the robustness of our analysis with respect to a change in the structure generation protocol, we have created two additional structural models for $Au_{102}(TBBT)_{44}$ and $Au_{92}(TBBT)_{44}$ by taking the initial coordinates of these two clusters, generated either via the docking procedure for $Au_{102}(TBBT)_{44}$ (mimicking as close as possible the hypothetical crystal structure of this cluster) or from the crystal coordinates for $Au_{92}(TBBT)_{44}$, and by performing a local relaxation at the DFT level, while keeping the AuS cores frozen. Using these new models, the energetics of the metal addition reaction does not qualitatively change, now being $\Delta E^{\text{interconv}} = -0.01$ eV, meaning that according to this different modeling the two clusters are isoenergetic, which—given the size of this systems—is qualitatively in tune with our previous analysis. In other words, despite the fact that these new crystal-like cluster structures have a rather different network of ligand–ligand interactions compared to those used in our analysis above, a substantial energetic proximity between the two clusters is confirmed. The coordinates and fragmentation energy terms of the previous (relaxed) and frozen-core structural models are provided in the Supporting Information (Table S1).

Electronic Structure and Stability of Au_{92} and Au_{102}. Further insights into the electronic structure and stability of the thiolate-ligand-capped Au_n (n = 92, 102) nanoclusters, have been gained through calculations using the density functional theory (DFT) method, employing the Vienna ab initio simulation package VASP.[71−74] The wave functions were expanded in a plane wave basis with a kinetic energy cutoff of 400 eV. The interaction between the atomic cores and the valence electrons was described by the projector augmented-wave (PAW) potential[75] (which includes relativistic corrections) and the exchange-correlation functional was described by the Perdew–Wang PW91 generalized gradient approximation (GGA).[76−78] Results for the relaxed model (further optimized with VASP) are given in Figures 5, 6, and S3; for frozen-core electroic structure results see the Supporting Information (in particular Figure S2A).

In Figure 5, we display for the energy-optimized X-ray determined $Au_{102}(SR)_{44}$ cluster the projected density of states, PDOS, i.e. the electronic density of states projected onto the angular momentum components, introduced in ref 79 (see STh1). In the calculations of the PDOS the TBBT capping ligand is modeled (for computational convenience) by thiol–phenyl, that is SR = *S*-phenyl; for PDOS results with the TBBT ligands, showing close similarity to those displayed in the text of the manuscript, see Figures S2B, S2C. We also display images of representative superatom orbitals, located at the bottom of the spectrum (having nodal structures of 1S, and 1D wave functions, respectively) and near the top of the spectrum (with a nodal patterns characteristic of 1G and 1H states); a vertical dashed line at $E - E_F = 0$ denotes the location of the midpoint between the highest occupied molecular orbital (HOMO, of 1G character) and the lowest unoccupied one (LUMO, of 1H character).

The first feature observed in the PDOS is the relatively large HOMO–LUMO energy gap (Δ_{HL} = 0.46 eV). Inspection of the electronic structure of the cluster and the orbitals' angular momentum symmetries (Figure 5) shows that, in agreement with an early proposal—introduced first in ref 79, termed as a

https://dx.doi.org/10.1021/acs.jpcc.9b08846
J. Phys. Chem. C 2020, 124, 1655−1666

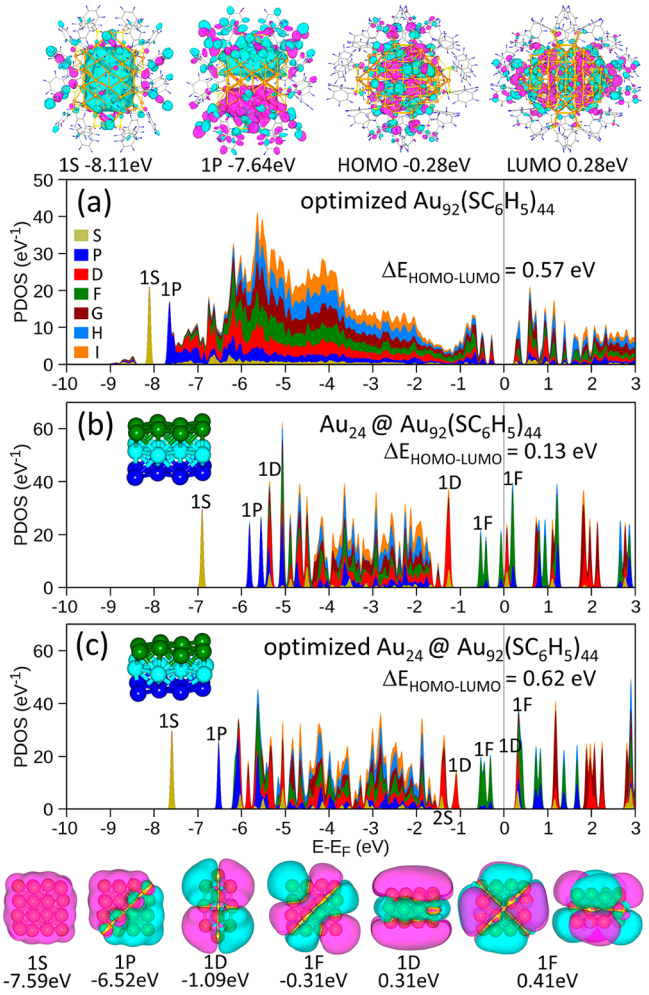

Figure 6. Calculated projected densities of states (PDOS) for (a) the $Au_{92}(S\text{-phenyl})_{44}$ cluster. Also shown are iso-surfaces of states at the bottom of the PDOS spectrum (marked 1S and 1P), and near the Fermi level (marked HOMO and LUMO). (b) The Au_{24} core in the geometry. It is found in the capped 92-gold-atom cluster, denoted as Au_{24}@ $Au_{92}(S\text{-phenyl})_{44}$. (c) The structurally relaxed Au_{24}@ $Au_{92}(S\text{-phenyl})_{44}$ core. Note the opening of the HOMO−LUMO gap (Δ_{HL}= 0.62 eV). Also shown at the bottom are iso-surfaces of superatom orbitals of the relaxed core (the two colors correspond to different signs of the wave function). The insets in parts b and c show the atomic arrangements in the 24-gold-atom core (different layers depicted by different color balls). The various angular momenta contribution to the PDOS are displayed in different colors, as given in the inset to part a.

"partial jellium" model, and used extensively in subsequent studies of ligand-protected metal clusters[18,45]—while for a wide range of energies (located at the middle of the energy spectrum), the electronic wave functions exhibit localized character (associated with Au atomic 5d electrons), and the orbitals of states with energies near the top (near the Fermi level) and bottom of the electronic spectrum are of delocalized character, derived from the atomic Au $6s^1$ electrons (see representative orbital images in Figure 5). These delocalized states can be assigned particular symmetries, determined with the use of an expansion of the calculated wave functions in spherical harmonics following[80] the electronic cluster-shell-model[80] (CSM). Associated with the CSM is a (superatom) aufbau rule: $1S^2|1P^6|1D^{10}|2S^2\ 1F^{14}|2P^6\ 1G^{18}|2D^{10}1H^{22}\ 3S^2|1I^{26}$..., where S, P, D, F, G, H, and I, correspond, respectively, to angular momenta, L = 0, 1, 2, 3, 4, 5, and 6. In the above CSM scheme, the vertical lines denote shell-closures (magic numbers), with closure near the Fermi level often accompanied by the opening of a stabilizing energy gap (refereed to in this paper as Δ_{HL}); in the above shell-structure scheme the shell closures occur at n^* = 2, 8, 18, 20 34, 58, 90, 92, ... electrons (with the values of n^*'s called "magic numbers"). The above shell-closure magic numbers apply to spherical (or near-spherical) clusters. Lifting of the $g = 2L+1$ degeneracy of levels belonging to the Lth angular momentum shell may occur for nonspherical clusters (particularly for states near the Fermi level, see below); for early use of such crystal-field splitting in the context of the electronic spectrum of the C_{60} cluster, see ref 81, and for a general discussion of cluster shape effects on the electronic shell model of metal clusers see ref 82.

In Figure 5 the occupied superatom spectrum consists of n^* = 58 delocalized electrons ($1S^2|1P^6|1D^{10}|2S^2\ 1F^{14}|2P^6\ 1G^{18}|$); this number of electrons equals the number of Au atoms in the cluster (102), less the number of sulfur-anchored ligands (44). The HOMO complex, ($2P^6$, $1G^{18}$) consisting of 12 orbitals and holding 24 electrons, and the LUMO complex (1H, 2D) consists of 16 (empty) orbitals. Deviations from spherical symmetry (of the cluster geometry and effective electronic potential) can cause certain alterations in level ordering, as well as splittings of the $(2L + 1)$-fold level degeneracy (of the L's superatom orbital) by crystal-field effects. Such splittings are seen clearly in the PDOS in Figure 5.

The PDOS for $Au_{92}(S\text{-phenyl})_{44}$ displayed in Figure 6a exhibits a HOMO−LUMO gap $\Delta_{HL=}$ 0.57 eV at the Fermi level. Furthermore, the PDOS shows clear evidence for a superatom CSM structure at the bottom of the spectrum (see features marked as 1S and 1P), whereas at the top of the PDOS (in the HOMO and LUMO regions) the spectrum is more complex. Indeed, the displayed orbitals' isosurfaces corresponding to states at the bottom of the spectrum show well-developed 1S and 1P delocalized wave functions of delocalized superatom character, whereas those at the top of the spectrum (labeled HOMO and LUMO; see Figure 6a) are of mixed (hybridized) nature (see also Figures S1 and S3, and Table S2). We remark here that even though the 1S and 1P states portray clear delocalized superatom character, they also show some (small) mixing with capping ligand orbitals (see the 1S and 1P wave functions above Figure 6a). These hybridized components were not included in the integration involved in calculation of the PDOS (see Supporting Information section titled STh1. Projected Density of States) for the entire $Au_{92}(S\text{-phenyl})_{44}$ cluster, where a radius of integration R_0 = 5.5 Å was employed (which is large enough to include all the metal atoms of the cluster); this accounts for the somewhat lower amplitude of the superatom peaks (e.g., 1S and 1P) in Figure 6a than those for the bare Au_{24} cluster [for which there were no ligands, and an integration radius of R_0 = 9.5 Å was used, Figure 6b,c, while for the Au_{24} atom cluster, essentially the same PDOS plots as those in Figure 6b,c were obtained with R_0 = 5.5 Å]. Obviously, the above consideration does not effect the energy locations of the states in the PDOS plots.

To unravel the spectral behavior near the Fermi level, *we focus our attention on the inner core of the cluster, namely, on the 24 gold atoms which are not directly bonded to any of the capping ligands* [see inset in Figure 6b, labeled Au_{24}@$Au_{92}(S\text{-phenyl})_{44}$]. The PDOS for that core region (in the geometry it has as part of the capped 92 gold atom cluster) shows a small Δ_{HL}= 0.13 eV and a crowding of several states near the Fermi

https://dx.doi.org/10.1021/acs.jpcc.9b08846
J. Phys. Chem. C 2020, 124, 1655−1666

level (see Figure 6b). On the other hand, structural relaxation of the 24-atom core results in opening of a large gap (Δ_{HL} = 0.62 eV) and a clear superatom structure in the bottom part of the spectrum as well as at the HOMO and LUMO regions [see Figure 6c, and the superatom orbital iso-surfaces at the bottom]. Inspection of the occupancies of the various energy levels shows that of the five 1D orbitals four lie below the Fermi level (accommodating eight electrons), and the other 1D level is shifted to the unoccupied manifold. Furthermore, out of the seven 1F superatom orbitals, three lie below the Fermi level, occupying 6 electrons and the rest of the 1F levels are shifted above E_F joining the unoccupied manifold. As a result the gapped electronic structure (that is, the above-noted Δ_{HL} = 0.62 eV gap) of the relaxed $Au_{24}@Au_{92}(S\text{-phenyl})_{44}$] core cluster, is described by the superatom energy level sequence: $1S^2|1P^6|2S^2\ 1D^8|1F^6$ (occupied by 24 electrons). We reiterate that the above splitting and shifting of superatom orbitals in the HOMO and LUMO region result from the nonspherical geometry of the 24-atom core cluster. Note that here the stabilization energy gap does not occur for one of the aforementioned magic-number, n^*, that correspond to spherical-shell closures. Instead, because of the degenarcy lifting (splitting) due to the prounced nonspherical symmetry of the 24-Au-atom inner-core cluster (see inset in Figure 6b,c), the gap opens inside the 1D and 1F angular momentum shells (at the top of the occupied spectrum, near E_F), with only some of the levels of these shells being occupied (i.e., lying below E_F), while the other levels shift to higher energy (above E_F) belonging the unoccupied manifold above the stabilization gap (see Figure 6c).

As aforementioned the results in Figures 5, 6, S1, and S3 and Table S2a,c were obtained for the relaxed model discussed in the Results and Discussion, subsection titled "Energy Decomposition and System Comparison Analyses", and further optimized with the use of the VASP DFT simulation package. PDOS results for the "frozen core" structural model (described in the last paragraph of the subsection Energy Decomposition and System Comparison Analyses) with the coordinates listed in the Supporting Information, are given, respectively, in Figure S2a,b for the capped 102 and 92 gold clusters (with the TBBT ligands modeled by *S*-phenyl, where only the H atoms replacing the terbutyl group were VASP-optimized optimized). These results portray the robustness of the structural models to variations in the computational preparation and optimization (an issue of particular importance for the 102 gold atom cluster where crystallographic data is available only for the *p*-mercaptobenzoic acid ligands, that is the $Au_{102}(p\text{-MBA})_{44}$ system, as discussed earlier in this paper). These calculated results show a close overall similarity between the electronic PDOS of the two structural models, with the HOMO−LUMO gaps for the "frozen model" being somewhat smaller than those calculated for the fully relaxed one: that is, 0.32 eV (0.46 eV) and 0.54 eV (0.57 eV)) for the frozen-core $Au_n(SR)_{44}$, n = 102 and 44, respectively (with the values for the fully relaxed systems given in parentheses), the difference being smaller for the 92-Au atom cluster.

The states displayed near the Fermi-level for the two cluster sizes (compare, respectively, Figures 5 and 6a with those in Figure S2a,b, calculated for the two structural models, varying mainly by their ligands configurations), are dominated by the same superatom angular momenta, for the two ligand-relaxation modes, as shown in Table S2b,d. This serves as further evidence regarding the robustness of the underlying supershell structure that acts as a stabilizing factor; for the smaller, 92-gold atom cluster, the amplitudes of the superatom states near the Fermi-level are lower than those found for the larger, 102-Au-atom cluster. This is due to stronger perturbation in the smaller cluster (and subsequent orbital distortion and hybridization) caused by the outer gold atom shells that anchor the capping ligands. As described above, these perturbing effects can be unraveled through the introduced CCSM model (see the progression in Figure 6a−c). Further support for the proposed CCSM derives from examination of the "orbital tomography" shown in Figure S3, which reflects the localization (anchoring) of the superatom orbitals (1S, 1P, ...) on the FCC- stacked Au24 inner-core, denoted above as $Au_{24}@\ Au_{92}(S\text{-phenyl}_3)_{44}$ (see upper panel of Figure 1 and inserts in Figure 6b,c).

Finally, we remark here that the above analysis, which we term as "core-cluster shell-model" (CCSM) introduces a new conceptual element, where the electronic stabilization (evidenced by a finite HOMO−LUMO gap) is traced to, and derives from, the superatom electronic shell organization of the energy levels in an inner core region of the ligand-capped cluster [here the $Au_{24}@Au_{92}(S\text{-phenyl})_{44}$].

It is pertinent to comment here that the superatom model of a metal cluster, pertains to organization of the valence electrons (the $6s^1$ electrons in the case of gold cluster) into delocalized states (the superatom states), which describe the motion of these electrons under the influence of the cluster's effective mean-field potential (see, e.g, ref 79). For a (neutral) bare metal M (e.g., M= Au, Ag) cluster,[79] the number (N_v) of valence electrons to be considered equals the number of metal atoms, N_A. On the other hand in the case of an organically capped metal cluster $M_{NA}(SR)_m$, $N_v = N_A - m$ (accounting for the bonding of the m thiolate ligands to the metal cluster).[18,45] The CCSM introduced here aims at explaining the stability of capped clusters where the above prescription does not yield a satisfactory explanation; namely, cases where no energy gap is found near E_F, or when the states near E_F (e.g., the HOMO and LUMO states, and those in their vicinity) do not show a delocalized (superatom) character (see Figure 6a). The CCSM generalizes the above prescription by assigning the superatom stabilization only to the inner-core region of the capped metal cluster, comprised only of gold atoms which are *not bonded directly* to the S atoms of the thiol ligands; for the $Au_{92}(TBBT)_{44}$ cluster considered here, this inner core consists of the 24-Au atoms (with N_v = 24) shown in column a of the top panel of Figure 1 (see also inset in Figure 6b,c).

Focusing on the electronic structure of the inner-core region is motivated, in part, by the expectation that from a cluster-growth perspective it is expected that the stability of the early formed inner core of the metal cluster, in particular, its superatom shell structure and the stabilization that it provides, would be maintained (at least in large part) and be imparted to the assembling outer atomic shells comprised of metal atoms that interact and anchor the capping (protecting) organic ligands. We expect this mode of analysis to be most useful in investigations of a broad range of nanocluster systems (particularly in the larger cluster range), including cases where the density of states of the entire capped cluster shows only a small, or no, HOMO−LUMO gap.

CONCLUSIONS

Au_{92} nanomolecules possess an untwinned FCC structure whereas Au_{102} has a 5-fold twinned structure. Despite these

https://dx.doi.org/10.1021/acs.jpcc.9b08846
J. Phys. Chem. C 2020, 124, 1655−1666

significant diverse structural motifs of the metal cores and the complexities of the interfacial staples that anchor the organic (TBBT) ligands, both clusters were found here to have the same number of ligands. In the case of the Au_{92} nanocluster molecule the capping monolayer is primarily composed of bridging ligands (~64%) and the rest appear as in staple motifs, whereas the Au_{102} nanocluster is protected solely by staple motifs. The staple-motif configurations seems to play a vital role in dictating the structure and composition of the nanocluster molecules.

First-principles electronic structure computational modeling via fragmentation and system comparison analysis indicate that despite the major difference between the two nanomolecules, the energetic stability is very similar between the two nanomolecule systems, with merely a ~1 eV difference between the two. The optical absorption study of $Au_{102-104}$ reveals featureless spectra, whereas Au_{92} has distinct absorption bands.

Analyses of the DFT-calculated angular-momentum−projected density of states (PDOS) spectra provide deep insights into the superatom cluster-shell-model (CSM) organization of the electronic energy levels, with the TBBT-capped Au_{102} system showing a 58-electron superatom shell-closing and a 0.46 eV HOMO−LUMO stabilizing energy gap. The stability of the TBBT-capped Au_{92} nanocluster molecule is elucidated through the newly introduced "core cluster shell model" (CCSM) where the superatom shell closing and gap (~0.6 eV) opening is found here to originate from the electronic structure of the FCC inner metallic core, Au_{24}@ Au_{92}(*S*-phenyl)$_{44}$, of the nanomolecule. In both the ligand-capped Au_{92} and Au_{102} clusters, added structural stabilization is gained through interfacial staple-anchoring to the metal cluster and ligand organization.

EXPERIMENTAL SECTION

Materials. Hydrogen tetrachloroaurate (III) ($HAuCl_4.3H_2O$) (Alfa Aesar ACS grade), sodium borohydride ($NaBH_4$) (Sigma-Aldrich, 99%), 2-phenylethanethiol (Sigma-Aldrich, 98%), 4-methylbenzenethiol (Sigma-Aldrich, 98%), 4-*tert*-butylbenzenethiol (TBBT) (TCI America, > 97%), and *trans*-2-[3[(4-*tert*-butyl phenyl)-2-methyl-2-propenylidene]-malononitrile (DCTB matrix) (TCI America) were used as received. HPLC grade solvents such as tetrahydrofuran, toluene, and methanol were purchased from Fisher Scientific. All materials were used as received.

Synthesis. Synthesis of $Au_{102-104}(TBBT)_{44-46}$ was performed in three steps. First, $Au_{144}(SCH_2CH_2Ph)_{60}$ was synthesized and then core-converted to Au_{99} by reacting with 4-methylbenzenethiol.[27] Finally, $Au_{99}(SR)_{42}$ was then reacted with TBBT (1 mg:100 μL of TBBT) for 1 h at room temperature under stirring to obtain $Au_{102-104}(TBBT)_{44-46}$. The reaction was then stopped by adding excess methanol and centrifuged at 4000 rpm for 3 min. The precipitate was washed with methanol (4×) to remove the excess thiol. Re-etching was carried out for 15 min if few unexchanged ligands were present.

Instrumentation. A Voyager DE PRO mass spectrometer was used to acquire MALDI-TOF mass spectra using DCTB matrix. Electrospray ionization mass spectra (ESI-MS) were collected using a Waters Synapt HDMS instrument with THF as the solvent. UV−vis absorption spectra were collected using a Shimadzu UV-1601 spectrophotometer with toluene as the solvent.

ASSOCIATED CONTENT

Supporting Information

The Supporting Information is available free of charge at https://pubs.acs.org/doi/10.1021/acs.jpcc.9b08846.

Energy terms for comparison, PDOS description, Au_{92} HOMO−LUMO different views, angular momentum components weights, and cluster structures according to two different structure generation procedures as discussed in the text (PDF)

AUTHOR INFORMATION

Corresponding Authors

Uzi Landman − *Georgia Institute of Technology, Atlanta, Georgia;* orcid.org/0000-0002-1586-1554; Email: uzi.landman@physics.gatech.edu

Alessandro Fortunelli − *Consiglio Nazionale delle Ricerche, Pisa, Italy;* orcid.org/0000-0001-5337-4450; Email: alessandro.fortunelli@cnr.it

Amala Dass − *University of Mississippi, Oxford, Mississippi;* orcid.org/0000-0001-6942-5451; Email: amal@olemiss.edu

Other Authors

Naga Arjun Sakthivel − *University of Mississippi, Oxford, Mississippi;* orcid.org/0000-0001-8134-905X

Luca Sementa − *Consiglio Nazionale delle Ricerche, Pisa, Italy*

Bokwon Yoon − *Georgia Institute of Technology, Atlanta, Georgia*

Complete contact information is available at: https://pubs.acs.org/10.1021/acs.jpcc.9b08846

Notes

The authors declare no competing financial interest.

ACKNOWLEDGMENTS

NSF-CHE-1808138 and NSF-CHE-1255519 supported the work performed by N.A.S. and A.D. The work of B.Y. and U.L. has been supported by a grant from the Air Force Office of Scientific Research (AFOSR) under Award No. FA9550-15-1-0519. Calculations were carried out in part (VASP calculations) at the GATECH Center for Computational Materials Science. Computational support from the Cineca Supercomputing Center, Italy, is also gratefully acknowledged.

REFERENCES

(1) Brust, M.; Walker, M.; Bethell, D.; Schiffrin, D. J.; Whyman, R. Synthesis of Thiol-Derivatised Gold Nanoparticles in a Two-Phase Liquid-Liquid System. *J. Chem. Soc., Chem. Commun.* **1994**, *0*, 801−802.

(2) Whetten, R. L.; Khoury, J. T.; Alvarez, M. M.; Murthy, S.; Vezmar, I.; Wang, Z. L.; Stephens, P. W.; Cleveland, C. L.; Luedtke, W. D.; Landman, U. Nanocrystal gold molecules. *Adv. Mater.* **1996**, *8*, 428−433.

(3) Hostetler, M. J.; Green, S. J.; Stokes, J. J.; Murray, R. W. Monolayers in Three Dimensions: Synthesis and Electrochemistry of ω-Functionalized Alkanethiolate-Stabilized Gold Cluster Compounds. *J. Am. Chem. Soc.* **1996**, *118*, 4212−4213.

(4) Chen, S.; Ingram, R. S.; Hostetler, M. J.; Pietron, J. J.; Murray, R. W.; Schaaff, T. G.; Khoury, J. T.; Alvarez, M. M.; Whetten, R. L. Gold Nanoelectrodes of Varied Size: Transition to Molecule-Like Charging. *Science* **1998**, *280*, 2098−2101.

(5) Quinn, B. M.; Liljeroth, P.; Ruiz, V.; Laaksonen, T.; Kontturi, K. Electrochemical Resolution of 15 Oxidation States for Monolayer Protected Gold Nanoparticles. *J. Am. Chem. Soc.* **2003**, *125*, 6644−6645.
(6) Murray, R. W. Nanoelectrochemistry: Metal Nanoparticles, Nanoelectrodes, and Nanopores. *Chem. Rev.* **2008**, *108*, 2688−2720.
(7) Schaaff, T. G.; Shafigullin, M. N.; Khoury, J. T.; Vezmar, I.; Whetten, R. L.; Cullen, W. G.; First, P. N.; Gutiérrez-Wing, C.; Ascensio, J.; Jose-Yacamán, M. J. Isolation of Smaller Nanocrystal Au Molecules: Robust Quantum Effects in Optical Spectra. *J. Phys. Chem. B* **1997**, *101*, 7885−7891.
(8) Link, S.; El-Sayed, M. A.; Gregory Schaaff, T.; Whetten, R. L. Transition from Nanoparticle to Molecular Behavior: A Femtosecond Transient Absorption Study of A Size-Selected 28 atom Gold Cluster. *Chem. Phys. Lett.* **2002**, *356*, 240−246.
(9) Kwak, K.; Thanthirige, V. D.; Pyo, K.; Lee, D.; Ramakrishna, G. Energy Gap Law for Exciton Dynamics in Gold Cluster Molecules. *J. Phys. Chem. Lett.* **2017**, *8*, 4898−4905.
(10) Thanthirige, V. D.; Sinn, E.; Wiederrecht, G. P.; Ramakrishna, G. Unusual Solvent Effects on Optical Properties of Bi-Icosahedral Au_{25} Clusters. *J. Phys. Chem. C* **2017**, *121*, 3530−3539.
(11) Weissker, H. C.; Escobar, H. B.; Thanthirige, V. D.; Kwak, K.; Lee, D.; Ramakrishna, G.; Whetten, R. L.; López-Lozano, X. Information on Quantum States Pervades the Visible Spectrum of the Ubiquitous $Au_{144}(SR)_{60}$ Gold Nanocluster. *Nat. Commun.* **2014**, *5*, 3785.
(12) Chakraborty, I.; Pradeep, T. Atomically Precise Clusters of Noble Metals: Emerging Link between Atoms and Nanoparticles. *Chem. Rev.* **2017**, *117*, 8208−8271.
(13) Jadzinsky, P. D.; Calero, G.; Ackerson, C. J.; Bushnell, D. A.; Kornberg, R. D. Structure of a Thiol Monolayer-Protected Gold Nanoparticle at 1.1 Å Resolution. *Science* **2007**, *318*, 430−433.
(14) Heaven, M. W.; Dass, A.; White, P. S.; Holt, K. M.; Murray, R. W. Crystal Structure of the Gold Nanoparticle $[N(C_8H_{17})_4][Au_{25}(SCH_2CH_2Ph)_{18}]$. *J. Am. Chem. Soc.* **2008**, *130*, 3754−3755.
(15) Wong, O. A.; Hansen, R. J.; Ni, T. W.; Heinecke, C. L.; Compel, W. S.; Gustafson, D. L.; Ackerson, C. J. Structure-Activity Relationships for Biodistribution, Pharmacokinetics, and Excretion of Atomically Precise Nanoclusters in a Murine Model. *Nanoscale* **2013**, *5*, 10525−10533.
(16) Gao, Y.; Shao, N.; Zeng, X. C. Ab Initio Study of Thiolate-Protected Au_{102} Nanocluster. *ACS Nano* **2008**, *2*, 1497−1503.
(17) Lahtinen, T.; Hulkko, E.; Sokołowska, K.; Tero, T.-R.; Saarnio, V.; Lindgren, J.; Pettersson, M.; Häkkinen, H.; Lehtovaara, L. Covalently Linked Multimers of Gold Nanoclusters $Au_{102}(p\text{-MBA})_{44}$ and $Au_{\sim 250}(p\text{-MBA})_n$. *Nanoscale* **2016**, *8*, 18665−18674.
(18) Walter, M.; Akola, J.; Lopez-Acevedo, O.; Jadzinsky, P. D.; Calero, G.; Ackerson, C. J.; Whetten, R. L.; Grönbeck, H.; Häkkinen, H. A Unified View of Ligand-Protected Gold Clusters as Superatom Complexes. *Proc. Natl. Acad. Sci. U. S. A.* **2008**, *105*, 9157−9162.
(19) Hulkko, E.; Lopez-Acevedo, O.; Koivisto, J.; Levi-Kalisman, Y.; Kornberg, R. D.; Pettersson, M.; Häkkinen, H. Electronic and Vibrational Signatures of the $Au_{102}(p\text{-MBA})_{44}$ Cluster. *J. Am. Chem. Soc.* **2011**, *133*, 3752−3755.
(20) Pei, Y.; Zeng, X. C. Investigating The Structural Evolution of Thiolate Protected Gold Clusters from First-Principles. *Nanoscale* **2012**, *4*, 4054−4072.
(21) Salorinne, K.; Lahtinen, T.; Malola, S.; Koivisto, J.; Häkkinen, H. Solvation Chemistry of Water-Soluble Thiol-Protected Gold Nanocluster Au_{102} from DOSY NMR Spectroscopy and DFT Calculations. *Nanoscale* **2014**, *6*, 7823−7826.
(22) Mustalahti, S.; Myllyperkiö, P.; Malola, S.; Lahtinen, T.; Salorinne, K.; Koivisto, J.; Häkkinen, H.; Pettersson, M. Molecule-like Photodynamics of $Au_{102}(p\text{MBA})_{44}$ Nanocluster. *ACS Nano* **2015**, *9*, 2328−2335.
(23) Stark, M. C.; Baikoghli, M. A.; Lahtinen, T.; Malola, S.; Xing, L.; Nguyen, M.; Nguyen, M.; Sikaroudi, A.; Marjomäki, V.; Häkkinen, H.; Cheng, R. H. Structural Characterization of Site-Modified Nanocapsid with Monodispersed Gold Clusters. *Sci. Rep.* **2017**, *7*, 17048.
(24) Levi-Kalisman, Y.; Jadzinsky, P. D.; Kalisman, N.; Tsunoyama, H.; Tsukuda, T.; Bushnell, D. A.; Kornberg, R. D. Synthesis and Characterization of $Au_{102}(p\text{-MBA})_{44}$ Nanoparticles. *J. Am. Chem. Soc.* **2011**, *133*, 2976−2982.
(25) Rambukwella, M.; Sementa, L.; Barcaro, G.; Fortunelli, A.; Dass, A. Organosoluble $Au_{102}(SPh)_{44}$ Nanomolecules: Synthesis, Isolation, Compositional Assignment, Core Conversion, Optical Spectroscopy, Electrochemistry, and Theoretical Analysis. *J. Phys. Chem. C* **2015**, *119*, 25077−25084.
(26) Chen, Y.; Wang, J.; Liu, C.; Li, Z.; Li, G. Kinetically Controlled Synthesis of $Au_{102}(SPh)_{44}$ Nanoclusters and Catalytic Application. *Nanoscale* **2016**, *8*, 10059−10065.
(27) Nimmala, P. R.; Dass, A. $Au_{99}(SPh)_{42}$ Nanomolecules: Aromatic Thiolate Ligand Induced Conversion of $Au_{144}(SCH_2CH_2Ph)_{60}$. *J. Am. Chem. Soc.* **2014**, *136*, 17016−17023.
(28) Dass, A.; Nimmala, P. R.; Jupally, V. R.; Kothalawala, N. $Au_{103}(SR)_{45}$, $Au_{104}(SR)_{45}$, $Au_{104}(SR)_{46}$ and $Au_{105}(SR)_{46}$ Nanoclusters. *Nanoscale* **2013**, *5*, 12082−12085.
(29) Negishi, Y.; Nakazaki, T.; Malola, S.; Takano, S.; Niihori, Y.; Kurashige, W.; Yamazoe, S.; Tsukuda, T.; Häkkinen, H. A Critical Size for Emergence of Nonbulk Electronic and Geometric Structures in Dodecanethiolate-Protected Au Clusters. *J. Am. Chem. Soc.* **2015**, *137*, 1206−1212.
(30) Cleveland, C. L.; Landman, U. The Energetics and Structure of Nickel Clusters: Size Dependence. *J. Chem. Phys.* **1991**, *94*, 7376−7396.
(31) Sakthivel, N. A.; Dass, A. Aromatic Thiolate-Protected Series of Gold Nanomolecules and a Contrary Structural Trend in Size Evolution. *Acc. Chem. Res.* **2018**, *51*, 1774−1783.
(32) Yang, H.; Wang, Y.; Chen, X.; Zhao, X.; Gu, L.; Huang, H.; Yan, J.; Xu, C.; Li, G.; Wu, J.; Edwards, A. J.; Dittrich, B.; Tang, Z.; Wang, D.; Lehtovaara, L.; Häkkinen, H.; Zheng, N. Plasmonic Twinned Silver Nanoparticles with Molecular Precision. *Nat. Commun.* **2016**, *7*, 12809.
(33) Liu, J.-Y.; Alkan, F.; Wang, Z.; Zhang, Z.-Y.; Kurmoo, M.; Yan, Z.; Zhao, Q.-Q.; Aikens, C. M.; Tung, C.-H.; Sun, D. Different Silver Nanoparticles in One Crystal: $Ag_{210}(i\text{PrPhS})_{71}(Ph_3P)_5Cl$ and $Ag_{211}(i\text{PrPhS})_{71}(Ph_3P)_6Cl$. *Angew. Chem., Int. Ed.* **2019**, *58*, 195−199.
(34) Yan, J.; Zhang, J.; Chen, X.; Malola, S.; Zhou, B.; Selenius, E.; Zhang, X.; Yuan, P.; Deng, G.; Liu, K.; Su, H.; Teo, B. K.; Häkkinen, H.; Zheng, L.; Zheng, N. Thiol-Stabilized Atomically Precise, Superatomic Silver Nanoparticles for Catalysing Cycloisomerization of Alkynyl Amines. *Natl. Sci. Rev.* **2018**, *5*, 694−702.
(35) Song, Y.; Lambright, K.; Zhou, M.; Kirschbaum, K.; Xiang, J.; Xia, A.; Zhu, M.; Jin, R. Large-Scale Synthesis, Crystal Structure, and Optical Properties of the $Ag_{146}Br_2(SR)_{80}$ Nanocluster. *ACS Nano* **2018**, *12*, 9318−9325.
(36) Negishi, Y.; Sakamoto, C.; Ohyama, T.; Tsukuda, T. Synthesis and the Origin of the Stability of Thiolate-Protected Au_{130} and Au_{187} Clusters. *J. Phys. Chem. Lett.* **2012**, *3*, 1624−1628.
(37) Tlahuice-Flores, A.; Santiago, U.; Bahena, D.; Vinogradova, E.; Conroy, C. V.; Ahuja, T.; Bach, S. B. H.; Ponce, A.; Wang, G.; José-Yacamán, M.; Whetten, R. L. Structure of the Thiolated Au_{130} Cluster. *J. Phys. Chem. A* **2013**, *117*, 10470−10476.
(38) Dass, A.; Theivendran, S.; Nimmala, P. R.; Kumara, C.; Jupally, V. R.; Fortunelli, A.; Sementa, L.; Barcaro, G.; Zuo, X.; Noll, B. C. $Au_{133}(SPh\text{-}t\text{Bu})_{52}$ Nanomolecules: X-ray Crystallography, Optical, Electrochemical, and Theoretical Analysis. *J. Am. Chem. Soc.* **2015**, *137*, 4610−4613.
(39) Yan, J.; Malola, S.; Hu, C.; Peng, J.; Dittrich, B.; Teo, B. K.; Häkkinen, H.; Zheng, L.; Zheng, N. Co-Crystallization of Atomically Precise Metal Nanoparticles Driven by Magic Atomic and Electronic Shells. *Nat. Commun.* **2018**, *9*, 3357.
(40) Vergara, S.; Lukes, D. A.; Martynowycz, M. W.; Santiago, U.; Plascencia-Villa, G.; Weiss, S. C.; de la Cruz, M. J.; Black, D. M.; Alvarez, M. M.; López-Lozano, X.; Barnes, C. O.; Lin, G.; Weissker, H.-C.; Whetten, R. L.; Gonen, T.; Yacaman, M. J.; Calero, G.

https://dx.doi.org/10.1021/acs.jpcc.9b08846
J. Phys. Chem. C 2020, 124, 1655−1666

MicroED Structure of Au_{146}(p-MBA)$_{57}$ at Subatomic Resolution Reveals a Twinned FCC Cluster. *J. Phys. Chem. Lett.* **2017**, *8*, 5523−5530.
(41) Sakthivel, N. A.; Theivendran, S.; Ganeshraj, V.; Oliver, A. G.; Dass, A. Crystal Structure of Faradaurate-279: Au_{279}(SPh-*t*Bu)$_{84}$ Plasmonic Nanocrystal Molecules. *J. Am. Chem. Soc.* **2017**, *139*, 15450−15459.
(42) Lei, Z.; Li, J.-J.; Wan, X.-K.; Zhang, W.-H.; Wang, Q.-M. Isolation and Total Structure Determination of an All-Alkynyl-Protected Gold Nanocluster Au_{144}. *Angew. Chem., Int. Ed.* **2018**, *57*, 8639−8643.
(43) Yan, N.; Xia, N.; Liao, L.; Zhu, M.; Jin, F.; Jin, R.; Wu, Z. Unraveling the Long-Pursued Au_{144} Structure by X-Ray Crystallography. *Sci. Adv.* **2018**, *4*, No. eaat7259.
(44) Hossain, S.; Niihori, Y.; Nair, L. V.; Kumar, B.; Kurashige, W.; Negishi, Y. Alloy Clusters: Precise Synthesis and Mixing Effects. *Acc. Chem. Res.* **2018**, *51*, 3114−3124.
(45) Desireddy, A.; Conn, B. E.; Guo, J.; Yoon, B.; Barnett, R. N.; Monahan, B. M.; Kirschbaum, K.; Griffith, W. P.; Whetten, R. L.; Landman, U.; Bigioni, T. P. Ultrastable Silver Nanoparticles. *Nature* **2013**, *501*, 399−402.
(46) Tang, Q.; Hu, G.; Fung, V.; Jiang, D.-e. Insights into Interfaces, Stability, Electronic Properties, and Catalytic Activities of Atomically Precise Metal Nanoclusters from First Principles. *Acc. Chem. Res.* **2018**, *51*, 2793−2802.
(47) Agrachev, M.; Ruzzi, M.; Venzo, A.; Maran, F. Nuclear and Electron Magnetic Resonance Spectroscopies of Atomically Precise Gold Nanoclusters. *Acc. Chem. Res.* **2019**, *52*, 44−52.
(48) Whetten, R. L.; Weissker, H.-C.; Pelayo, J. J.; Mullins, S. M.; López-Lozano, X.; Garzón, I. L. Chiral-Icosahedral (I) Symmetry in Ubiquitous Metallic Cluster Compounds (145A,60X): Structure and Bonding Principles. *Acc. Chem. Res.* **2019**, *52*, 34−43.
(49) Nieto-Ortega, B.; Bürgi, T. Vibrational Properties of Thiolate-Protected Gold Nanoclusters. *Acc. Chem. Res.* **2018**, *51*, 2811−2819.
(50) Tlahuice-Flores, A. New Polyhedra Approach To Explain the Structure and Evolution on Size of Thiolated Gold Clusters. *J. Phys. Chem. C* **2019**, *123*, 10831−10841.
(51) Rambukwella, M.; Sakthivel, N. A.; Delcamp, J. H.; Sementa, L.; Fortunelli, A.; Dass, A. Ligand Structure Determines Nanoparticles' Atomic Structure, Metal-Ligand Interface and Properties. *Front. Chem.* **2018**, *6*, 330.
(52) Knoppe, S.; Dharmaratne, A. C.; Schreiner, E.; Dass, A.; Bürgi, T. Ligand Exchange Reactions on Au_{38} and Au_{40} Clusters: A Combined Circular Dichroism and Mass Spectrometry Study. *J. Am. Chem. Soc.* **2010**, *132*, 16783−16789.
(53) Zeng, C.; Liu, C.; Chen, Y.; Rosi, N. L.; Jin, R. Atomic Structure of Self-Assembled Monolayer of Thiolates on a Tetragonal Au_{92} Nanocrystal. *J. Am. Chem. Soc.* **2016**, *138*, 8710−8713.
(54) Liao, L.; Chen, J.; Wang, C.; Zhuang, S.; Yan, N.; Yao, C.; Xia, N.; Li, L.; Bao, X.; Wu, Z. Transition-Sized Au_{92} Nanoparticle Bridging Non-FCC-Structured Gold Nanoclusters and FCC-Structured Gold Nanocrystals. *Chem. Commun.* **2016**, *52*, 12036−12039.
(55) Eswaramoorthy, S. K.; Sakthivel, N. A.; Dass, A. Core Size Conversion of $Au_{329}(SCH_2CH_2Ph)_{84}$ to Au_{279}(SPh-*t*Bu)$_{84}$ Nanomolecules. *J. Phys. Chem. C* **2019**, *123*, 9634−9639.
(56) Higaki, T.; Liu, C.; Zhou, M.; Luo, T.-Y.; Rosi, N. L.; Jin, R. Tailoring the Structure of 58-Electron Gold Nanoclusters: $Au_{103}S_2$(S-Nap)$_{41}$ and Its Implications. *J. Am. Chem. Soc.* **2017**, *139*, 9994−10001.
(57) Dass, A. Nano-Scaling Law: Geometric Foundation of Thiolated Gold Nanomolecules. *Nanoscale* **2012**, *4*, 2260−2263.
(58) Love, J. C.; Estroff, L. A.; Kriebel, J. K.; Nuzzo, R. G.; Whitesides, G. M. Self-Assembled Monolayers of Thiolates on Metals as a Form of Nanotechnology. *Chem. Rev.* **2005**, *105*, 1103−1170.
(59) Crasto, D.; Barcaro, G.; Stener, M.; Sementa, L.; Fortunelli, A.; Dass, A. $Au_{24}(SAdm)_{16}$ Nanomolecules: X-ray Crystal Structure, Theoretical Analysis, Adaptability of Adamantane Ligands to Form $Au_{23}(SAdm)_{16}$ and $Au_{25}(SAdm)_{16}$, and Its Relation to $Au_{25}(SR)_{18}$. *J. Am. Chem. Soc.* **2014**, *136*, 14933−14940.
(60) Nimmala, P. R.; Theivendran, S.; Barcaro, G.; Sementa, L.; Kumara, C.; Jupally, V. R.; Apra, E.; Stener, M.; Fortunelli, A.; Dass, A. Transformation of $Au_{144}(SCH_2CH_2Ph)_{60}$ to Au_{133}(SPh-*t*Bu)$_{52}$ Nanomolecules: Theoretical and Experimental Study. *J. Phys. Chem. Lett.* **2015**, *6*, 2134−2139.
(61) Dass, A.; Jones, T. C.; Theivendran, S.; Sementa, L.; Fortunelli, A. Core Size Interconversions of Au_{30}(S-tBu)$_{18}$ and Au_{36}(SPhX)$_{24}$. *J. Phys. Chem. C* **2017**, *121*, 14914−14919.
(62) Rambukwella, M.; Sementa, L.; Fortunelli, A.; Dass, A. Core-Size Conversion of $Au_{38}(SCH_2CH_2Ph)_{24}$ to Au_{30}(S−tBu)$_{18}$ Nanomolecules. *J. Phys. Chem. C* **2017**, *121*, 14929−14935.
(63) Rambukwella, M.; Burrage, S.; Neubrander, M.; Baseggio, O.; Aprà, E.; Stener, M.; Fortunelli, A.; Dass, A. $Au_{38}(SPh)_{24}$: Au_{38} Protected with Aromatic Thiolate Ligands. *J. Phys. Chem. Lett.* **2017**, *8*, 1530−1537.
(64) Hutter, J.; Iannuzzi, M.; Schiffmann, F.; VandeVondele, J. CP2K: Atomistic Simulations of Condensed Matter Systems. *Wiley Interdiscip. Rev. Comput. Mol. Sci.* **2014**, *4*, 15−25.
(65) Goedecker, S.; Teter, M.; Hutter, J. Separable Dual-space Gaussian Pseudopotentials. *Phys. Rev. B: Condens. Matter Mater. Phys.* **1996**, *54*, 1703−1710.
(66) VandeVondele, J.; Hutter, J. Gaussian Basis Sets for Accurate Calculations on Molecular Systems in Gas and Condensed Phases. *J. Chem. Phys.* **2007**, *127*, 114105.
(67) Grimme, S.; Antony, J.; Ehrlich, S.; Krieg, H. A Consistent and Accurate Ab Initio Parametrization of Density Functional Dispersion Correction (DFT-D) for the 94 Elements H-Pu. *J. Chem. Phys.* **2010**, *132*, 154104.
(68) Perdew, J. P.; Burke, K.; Ernzerhof, M. Generalized Gradient Approximation Made Simple. *Phys. Rev. Lett.* **1996**, *77*, 3865−3868.
(69) Fihey, A.; Hettich, C.; Touzeau, J.; Maurel, F.; Perrier, A.; Köhler, C.; Aradi, B.; Frauenheim, T. SCC-DFTB Parameters for Simulating Hybrid Gold-Thiolates Compounds. *J. Comput. Chem.* **2015**, *36*, 2075−2087.
(70) Martyna, G. J.; Klein, M. L.; Tuckerman, M. Nosé−Hoover Chains: The Canonical Ensemble via Continuous Dynamics. *J. Chem. Phys.* **1992**, *97*, 2635−2643.
(71) Kresse, G.; Hafner, J. Ab Initio Molecular Dynamics for Liquid Metals. *Phys. Rev. B: Condens. Matter Mater. Phys.* **1993**, *47*, 558−561.
(72) Kresse, G.; Hafner, J. Ab Initio Molecular-Dynamics Simulation of The Liquid-Metal–Amorphous-Semiconductor Transition In Germanium. *Phys. Rev. B: Condens. Matter Mater. Phys.* **1994**, *49*, 14251−14269.
(73) Kresse, G.; Furthmüller, J. Efficient Iterative Schemes for Ab Initio Total-Energy Calculations using A Plane-Wave Basis Set. *Phys. Rev. B: Condens. Matter Mater. Phys.* **1996**, *54*, 11169−11186.
(74) Kresse, G.; Furthmüller, J. Efficiency of Ab-Initio Total Energy Calculations for Metals and Semiconductors using A Plane-Wave Basis Set. *Comput. Mater. Sci.* **1996**, *6*, 15−50.
(75) Kresse, G.; Joubert, D. From Ultrasoft Pseudopotentials to The Projector Augmented-Wave Method. *Phys. Rev. B: Condens. Matter Mater. Phys.* **1999**, *59*, 1758−1775.
(76) Perdew, J. P. In *Electronic Structure of Solids '91*; Akademie Verlag: Berlin, 1991.
(77) Perdew, J. P.; Chevary, J. A.; Vosko, S. H.; Jackson, K. A.; Pederson, M. R.; Singh, D. J.; Fiolhais, C. Atoms, Molecules, Solids, and Surfaces: Applications of The Generalized Gradient Approximation for Exchange and Correlation. *Phys. Rev. B: Condens. Matter Mater. Phys.* **1992**, *46*, 6671−6687.
(78) Perdew, J. P.; Chevary, J. A.; Vosko, S. H.; Jackson, K. A.; Pederson, M. R.; Singh, D. J.; Fiolhais, C. Erratum: Atoms, Molecules, Solids, and Surfaces: Applications of The Generalized Gradient Approximation for Exchange and Correlation. *Phys. Rev. B: Condens. Matter Mater. Phys.* **1993**, *48*, 4978−4978.
(79) Yoon, B.; Koskinen, P.; Huber, B.; Kostko, O.; von Issendorff, B.; Häkkinen, H.; Moseler, M.; Landman, U. Size-Dependent Structural Evolution and Chemical Reactivity of Gold Clusters. *ChemPhysChem* **2007**, *8*, 157−161.

https://dx.doi.org/10.1021/acs.jpcc.9b08846
J. Phys. Chem. C 2020, 124, 1655−1666

(80) Knight, W. D.; Clemenger, K.; de Heer, W. A.; Saunders, W. A.; Chou, M. Y.; Cohen, M. L. Electronic Shell Structure and Abundances of Sodium Clusters. *Phys. Rev. Lett.* **1984**, *52*, 2141−2143.
(81) Yannouleas, C.; Landman, U. Stabilized-jellium descript tion of neutral and multiply charged fullerenes $C_{60}^{x\pm}$. *Chem. Phys. Lett.* **1994**, *217*, 175−185.
(82) Yannouleas, C.; Landman, U. Electronic shell effects in triaxially deformed metal clusters: A systematic interpretation of experimental observations. *Phys. Rev. B: Condens. Matter Mater. Phys.* **1995**, *51*, 1902−1917.

https://dx.doi.org/10.1021/acs.jpcc.9b08846
J. Phys. Chem. C 2020, 124, 1655−1666